

First Results From New 3D Spectral Simulations Of Anelastic Turbulent Convection

Kaloyan Penev^a, Joseph Barranco^b, Dimitar Sasselov^c

^a60 Garden St., M.S. 10, Cambridge, MA 02138

^b1600 Holloway Avenue, San Francisco, CA 94132-4163

^c60 Garden St., M.S. 16, Cambridge, MA 02138

Abstract

We have adapted the anelastic spectral code of Barranco & Marcus (2006) to simulate a turbulent convective layer with the intention of studying the effectiveness of turbulent eddies in dissipating external shear (e.g. tides). We derive the anelastic equations, show the time integration scheme we use to evolve these equations and present the tests we ran to confirm that our code does what we expect. Further we apply a perturbative approach to find an approximate scaling of the effective eddy viscosity with frequency, and find that it is in general agreement with an estimate obtained by applying the same procedure to a realistic simulation of the upper layers of the solar convective zone.

Key words: Hydrodynamics, Anelastic approximation, Stratified flows, Shear flows, Spectral methods, Convection, Turbulence, Turbulent dissipation, Effective Viscosity

1. Introduction

Dissipation of stellar tides and oscillations is often considered to be mainly due to the turbulent flow in their convective zones. Usually the effects of the turbulent flow are parametrized by some sort of effective viscosity coefficient. Clearly the situation is not as simple as that and the usual “fix” is to allow this viscosity coefficient to depend on the perturbation being dissipated, most notably its frequency and perhaps direction of the shear it creates.

Completely analytical treatments start by assuming a Kolmogorov spectrum for the turbulent flow and combine it with some prescription for the effectiveness of eddies in dissipating perturbations of the given period. Since

Kolmogorov turbulence is isotropic the direction of shear is unimportant in such prescriptions. Two such prescriptions have been used.

The first, proposed by Zahn (1966, 1989), states that when the period of the perturbation (T) is shorter than the turnover times (τ) of some eddies, their dissipation efficiency should be proportional to the fraction of a churn they manage to complete in half a perturbation period, in other words, the effective viscosity coefficient scales like:

$$\nu = \nu_{max} \min \left[\left(\frac{T}{2\tau} \right), 1 \right]. \quad (1)$$

The second prescription is due to Goldreich & Nicholson (1977) and Goldreich & Keeley (1977). They argue that eddies with turnover times much bigger than the period of the perturbation will not contribute appreciably to the dissipation, and hence the effective viscosity should be dominated by the largest eddies with turnover times $\tau < T/2\pi$. Then the Kolmogorov prescription of turbulence predicts that the effective viscosity will scale as:

$$\nu = \nu_{max} \min \left[\left(\frac{T}{2\pi\tau} \right)^2, 1 \right] \quad (2)$$

Zahn's prescription has been tested against tidal circularization times for binaries containing a giant star (Verbunt & Phinney, 1995), and is in general agreement with observations. Also Zahn's prescription is in better agreement with observed tidal dissipation of binary stars in clusters (Meibom & Mathieu, 2005) and with the location of the red edge of the Cepheid instability strip (Gonczy, 1982).

The less efficient prescription has been used successfully by Goldreich & Keeley (1977), Goldreich & Kumar (1988) and Goldreich et al. (1994) to develop a theory for the damping of the solar p -modes. In this case the more effective dissipation would require dramatic changes in the excitation mechanism in order to explain the observed amplitudes.

Finally Goodman & Oh (1997) developed a perturbative derivation of the convective viscosity, which for a Kolmogorov scaling, gives a result that is closer to the less efficient Goldreich & Nicholson viscosity than it is to Zahn's. While providing a firmer theoretical basis for the former scaling, this does not resolve the observational problem of insufficient tidal dissipation.

The development of 2D and 3D simulations of solar convection hint at a possible resolution of this problem. The convective flow that these simulations predict is fundamentally very different from the assumed Kolmogorov

turbulence (Sofia & Chan, 1984; Stein & Nordlund, 1989; Malagoli et al., 1990). The first major difference is that the frequency power spectrum of the velocity field is much flatter than the Kolmogorov power spectrum, and hence one might expect that the dissipation will decrease significantly slower as frequency increases relative to the Kolmogorov case. Another major difference is that the velocity field is no longer isotropic and hence one would expect it to react differently to shear in different directions. That is, if we would use an effective viscosity coefficient, it should be a tensor and not a scalar quantity.

As a first step in investigating that possibility (Penev et al., 2007), we applied the perturbative approach developed by Goodman & Oh (1997) to a numerical model of solar convection (Robinson et al. 2003) to find the scaling of the components of the effective viscosity tensor with frequency. Somewhat unexpectedly, we found that the scaling closely follows Zahn’s prescription, even though when the same approach is applied to Kolmogorov turbulence it gives results closer to those of Goldreich and collaborators.

That left a lot of questions unanswered. For example, are the effects of turbulence anything at all like that of molecular viscosity, and is taking only the lowest order term in a power series expansion of the energy dissipation rate an acceptable approximation? The perturbative approach also assumes that the spatial scale of the external shear being dissipated is large compared to all convective scales, and hence can be assumed a linear function of position, but it would be interesting to see how quickly dissipation efficiency is lost as the spatial scale of the external shear decreases.

To tackle these questions we adapted the anelastic spectral code of Barranco & Marcus (2006) to simulate a convectively unstable box in which we are able to place external, time dependent shear as part of the evolution equations and observe the effects of the turbulent convective flow directly.

In order to make the code suitable to simulate convection we added heat diffusion, that allows for the supply the heat that will drive the convective motions. This in turn necessitated that we allow for a more general background state slightly modified treatment of the pressure and the introduction of temperature boundary conditions. In addition we added an external forcing term and removed the Keplerian shear and the accompanying it shearing coordinates.

The resulting code is ideal for our purposes for the following reasons:

1. The anelastic approximation means no shock or sound waves can exist

and hence the time steps can be much larger than for a fully compressible code, and yet the anelastic approximation allows phenomena such as convection to occur unlike in completely incompressible codes. This allows us to get much closer to the actual time scales of interest (usually of order hours or days) than a fully compressible code would. The Boussinesq approximation has those same properties, however it is not suitable for simulating stratified convection where the buoyancy does not depend entirely on the temperature.

2. Spectral codes are more efficient at simulating turbulent flows than finite difference codes because their spatial accuracy is exponential rather than a power law, so they are capable of reliably reproducing the turbulent flow even at modest resolution.
3. The grid happens to have higher density near the top and bottom of the box where it is needed in order to resolve the boundary layers that develop there due to the boundary conditions we impose.

In this paper we present the details of the modified code as well as a perturbative estimate of the efficiency of turbulent viscosity. In section 2 we derive the anelastic approximation to the Navier-Stokes equations modified to include a time dependent shear. In section 3 we present the numerical algorithm. In section 4 we show the tests we ran to confirm that our implementation actually evolves the desired equations, and verify that the numerical scheme is indeed second-order accurate in time. Finally, in section 5 we use a perturbative calculation to get an estimate of the effective turbulent viscosity in our simulated box.

2. The evolution equations

We define upfront the following quantities describing the fluid and the flow:

p – pressure	T – temperature
ρ – density	\mathbf{v} – velocity
θ – potential temperature	C_p – constant pressure specific heat
R – ideal gas constant	g – acceleration of gravity
κ – heat diffusion coefficient	\mathbf{f} – some external forcing (e.g. tidal force)

As was said before we do not actually evolve the fully compressible fluid equations but rather their anelastic approximation (c.f. Bannon (1996)).

Under the anelastic assumption each flow variable is split into a sum of a time-independent background component (denoted by an over bar) and a time varying perturbation (denoted by tilde over its symbol) superimposed on top of that.

The background variables satisfy the fully compressible equations with all x, y and t derivatives set to zero. The background velocity is assumed to be zero as well. The boundary conditions that complete these equations are that we require the background temperature on the top and bottom walls to have some fixed values T_l and T_h respectively, and the pressure at the top wall to have some value, p_{top} . Alternatively, we could fix the temperature gradients at the boundary, which would set the flux that the simulated convective layer must transport. Neither of those two options is exactly what the actual physical problem requires. We could base our boundary conditions on reliable physics if we were planning to simulate the entire convective zone. However, this is impossible to do at the resolution required to study the turbulent dissipation, so we will ultimately be interested only in the flow that develops in the interior of the box and plan to exclude the regions near the top and bottom boundary from any analysis we do. For this reason the choice of the exact thermal boundary conditions will hopefully have little impact on our results.

For convenience, we define the following quantities:

$$\mathcal{K}(z) \equiv \int_{-L_z/2}^z \frac{dz}{\kappa(z)} \quad (3)$$

$$\alpha \equiv \frac{T_h - T_l}{\mathcal{K}(L_z/2)} \quad (4)$$

Where the z coordinate has a value $-L_z/2$ at the bottom of the box and $L_z/2$ at the top of the box.

The background variables that emerge as the solution to fully compressible equations are:

$$\bar{T}(z) = T_h - \alpha \mathcal{K} \quad (5)$$

$$\bar{\rho}(z) = \frac{p_{top}}{R\bar{T}_l} \exp \left[\int_z^{L_z/2} \frac{1}{\bar{T}} \left(\frac{g}{R} - \frac{\alpha}{\kappa} \right) dz \right] \quad (6)$$

$$\bar{p} = \bar{\rho} R \bar{T} \quad (7)$$

$$\bar{\theta} = \bar{T} \left(\frac{p_0}{\bar{p}} \right)^{\frac{R}{c_p}} \quad (8)$$

With those definitions the anelastic equations governing the evolution of the perturbation variables become:

$$\nabla \cdot \bar{\rho} \mathbf{v} = 0 \quad (9)$$

$$\frac{\partial \mathbf{v}}{\partial t} = \mathbf{v} \times \boldsymbol{\omega} - \nabla \tilde{h} + \frac{\tilde{\theta}}{\bar{\theta}} g \hat{\mathbf{z}} + \mathbf{f} \quad (10)$$

$$\frac{\partial \tilde{\theta}}{\partial t} = -v_z \frac{d\bar{\theta}}{dz} - \mathbf{v} \cdot \nabla \tilde{\theta} + \frac{\bar{\theta}}{C_p \bar{T} \bar{\rho}} \nabla \cdot (\kappa \nabla \tilde{T}) \quad (11)$$

$$\tilde{h} \equiv \frac{\tilde{p}}{\bar{\rho}} + \frac{\mathbf{v}^2}{2} \quad (12)$$

$$\frac{\tilde{p}}{\bar{p}} = \frac{\tilde{\rho}}{\bar{\rho}} + \frac{\tilde{T}}{\bar{T}} \quad (13)$$

$$\frac{\tilde{\theta}}{\bar{\theta}} = \frac{\tilde{p}}{\bar{\rho} g H_\rho} - \frac{\tilde{\rho}}{\bar{\rho}} \quad (14)$$

Where we have introduced an enthalpy \tilde{h} (defined by equation 12), a density scale height $H_\rho \equiv -\left(\frac{d \ln \bar{\rho}}{dz}\right)^{-1}$ and the vorticity $\boldsymbol{\omega} \equiv \nabla \times \mathbf{v}$. Equation 14 is not the correct linearized equation for the potential temperature. The denominator of the pressure term should have been $\gamma \bar{p}$ instead of $\bar{\rho} g H_\rho$. This replacement was introduced by Bannon (1996). He showed that this substitution is required to ensure that the anelastic equations conserve energy. To define the time evolution completely we need to add boundary conditions to the above equations. The boundary conditions on the four vertical walls of the domain are set by the fact that we use Fourier series expansion for the horizontal spatial dependence of all quantities, and hence all quantities are naturally periodic in those directions. In addition to that, we want the temperature at the top and bottom boundary to be whatever we specify, and hence its perturbation should be zero. Also we require that the top and bottom walls are impermeable, but with no friction. That means that we set v_z to zero at the top and bottom boundary, and do not require anything for v_x and v_y .

The anelastic equations above obey a set of energy conservation equations for the following definitions of the kinetic and thermal energies:

$$E_K \equiv \int_V \bar{\rho} \frac{\mathbf{v}^2}{2} dV \quad (15)$$

$$E_T \equiv \int_V C_p \bar{\rho} \bar{T} \frac{\tilde{\theta}}{\bar{\theta}} dV \quad (16)$$

Using the anelastic evolution equations we can express the rates of change of these two energies to be:

$$\frac{dE_K}{dt} = \mathcal{E}_1 \quad (17)$$

$$\frac{dE_T}{dt} = -\mathcal{E}_1 + \mathcal{E}_2 \quad (18)$$

Where sinks/sources are defined as:

$$\mathcal{E}_1 \equiv g \int_V \frac{\bar{\rho}}{\bar{\theta}} \tilde{v} \tilde{\theta} dV \quad (19)$$

$$\mathcal{E}_2 \equiv \int \left(\kappa \frac{\partial \tilde{T}}{\partial z} \Big|_{\frac{L_z}{2}} - \kappa \frac{\partial \tilde{T}}{\partial z} \Big|_{-\frac{L_z}{2}} \right) dx dy \quad (20)$$

3. Numerical Time Evolution

3.1. Spectral Method

The spectral representation for a flow variable (q) used in the code is given by:

$$q(x, y, z, t) \approx \sum_{k=-\frac{N_x}{2}+1}^{\frac{N_x}{2}} \sum_{l=-\frac{N_y}{2}+1}^{\frac{N_y}{2}} \sum_{m=0}^{N_z} \hat{q}_{klm}(t) e^{i2\pi kx/L_x} e^{i2\pi ly/L_y} T_m(z) \quad (21)$$

Where the vertical basis functions: $T_m(z) \equiv \cos\left(m \cos^{-1} \frac{z}{L_z}\right)$, are Chebyshev polynomials. The spectral method we use does almost all calculations in the wavenumber/Chebyshev space, except for taking products of variables, which are done by first transforming back to physical (x, y, z) space on a grid of collocation points, taking the product there and transforming back. For a more complete discussion of the spectral method used see Barranco & Marcus (2006) (section 3 and 3.2).

3.2. Time integration

3.2.1. Advection Step

The advection step is fully explicit. It uses variables from this and the previous time step to achieve second order accuracy. It first calculates the quantities:

$$\mathfrak{M} \equiv \mathbf{v} \times \boldsymbol{\omega} + \frac{\tilde{\theta}}{\theta} g \hat{\mathbf{z}} \quad (22)$$

$$\mathfrak{N} \equiv -v_z \frac{d\tilde{\theta}}{dz} - \mathbf{v} \cdot \nabla \tilde{\theta} \quad (23)$$

Then velocity and temperature are updated using:

$$\mathbf{v}^{N+\frac{1}{3}} = \mathbf{v}^N + \frac{\Delta t}{2} (3\mathfrak{M}^N - \mathfrak{M}^{N-1}) \quad (24)$$

$$\tilde{\theta}^{N+\frac{1}{3}} = \tilde{\theta}^N + \frac{\Delta t}{2} (3\mathfrak{N}^N - \mathfrak{N}^{N-1}) \quad (25)$$

3.2.2. Hyperviscosity Step

The purpose of this step is to suppress the highest modes both in the horizontal and vertical directions to avoid buildup of power there due to the truncation of the spectrum at some finite number of spectral coefficients. For finite difference codes a step of this sort is unnecessary because there is some finite “grid viscosity” associated with the numerical scheme. In spectral codes there is no equivalent effect that prevents the build up of power at the highest simulated wavenumber modes. We implement the hyperviscosity step exactly in the way described in Barranco & Marcus (2006), suppressing each spectral coefficient by a factor as follows:

$$\mathbf{v}^{N+\frac{2}{3}} = \mathbf{v}^{N+\frac{1}{3}} \exp \left[-\Delta t \left(\nu_{\perp}^{hyp} k_{\perp}^{2p} + \nu_z^{hyp} m^{2p} \right) \right] \quad (26)$$

$$\theta^{N+\frac{2}{3}} = \theta^{N+\frac{1}{3}} \exp \left[-\Delta t \left(\nu_{\perp}^{hyp} k_{\perp}^{2p} + \nu_z^{hyp} m^{2p} \right) \right] \quad (27)$$

Where ν_{\perp}^{hyp} and ν_z^{hyp} are some hyperviscosity coefficients, p is an integer between 1 and 6. $k_{\perp}^2 \equiv k_x^2 + k_y^2$ is the horizontal wavenumber and n is the order of the Chebyshev polynomial that this particular amplitude applies to.

3.2.3. Pressure Step

The pressure step basically ensures that the velocity at the end of the time step satisfies the anelastic constraint. In the numerical scheme we abandon

the enthalpy at a specific time as a variable, and instead use its average between two consecutive time steps:

$$\Pi^{N+1} \equiv \frac{1}{2} \left(\tilde{h}^{N+1} + \tilde{h}^N \right) \quad (28)$$

We then achieve second order accurate time evolution by updating the velocity according to:

$$\mathbf{v}^{N+1} = \mathbf{v}^{N+\frac{2}{3}} - \frac{\Delta t}{2} \left(\nabla \tilde{h}^{N+1} + \nabla \tilde{h}^N \right) = \mathbf{v}^{N+\frac{2}{3}} - \Delta t \nabla \Pi^{N+1} \quad (29)$$

So imposing the anelastic constraint we get:

$$0 = \nabla \cdot \mathbf{v}^{N+1} + v_z^{N+1} \frac{d \log \bar{\rho}}{dz} = \nabla \cdot \mathbf{v}^{N+\frac{2}{3}} - \Delta t \nabla^2 \Pi^{N+1} + v_z^{N+\frac{2}{3}} \frac{d \log \bar{\rho}}{dz} - \Delta t \frac{\partial \Pi^{N+1}}{\partial z} \frac{d \log \bar{\rho}}{dz} \quad (30)$$

Regrouping and imposing $v_z|_{\pm L_z/2} = 0$ we get the differential equation for updating Π with its boundary conditions:

$$\left[\nabla^2 + \frac{d \log \bar{\rho}}{dz} \frac{\partial}{\partial z} \right] \Pi^{N+1} = \frac{1}{\Delta t} \left(\nabla \cdot \mathbf{v}^{N+\frac{2}{3}} + v_z^{N+\frac{2}{3}} \frac{d \log \bar{\rho}}{dz} \right) \quad (31)$$

$$\frac{\partial \Pi^{N+1}}{\partial z} \Big|_{\pm L_z/2} = \frac{1}{\Delta t} v_z^{N+\frac{2}{3}} \Big|_{\pm L_z/2} \quad (32)$$

For details of the implementation of this equation in our code see appendix A

3.2.4. Heat Diffusion Step

The heat diffusion step updates the potential temperature according to:

$$\tilde{\theta}^{N+1} = \tilde{\theta}^{N+\frac{2}{3}} + \frac{\Delta t \bar{\theta} R \kappa}{2 C_p \bar{p}} \left[\nabla^2 + \frac{d \ln \kappa}{dz} \frac{\partial}{\partial z} \right] \left(\tilde{T}^N + \tilde{T}^{N+1} \right) \quad (33)$$

When we express \tilde{T} in terms of \mathbf{v}, \tilde{h} and $\tilde{\theta}$, this gives a second order differential equation for $\tilde{\theta}^{N+1}$. In terms of the following definitions:

$$\mathfrak{P} \equiv -\frac{\alpha\bar{\theta}}{g\kappa\bar{T}} \left[\nabla^2 - \frac{d \ln \kappa}{dz} \frac{\partial}{\partial z} + \frac{\kappa'^2}{\kappa^2} - \frac{\kappa''}{\kappa} \right] \left(\tilde{h} - \frac{v^2}{2} \right) \quad (34)$$

$$C_1 \equiv \frac{d \ln \kappa}{dz} - \frac{2g}{C_p\bar{T}} \quad (35)$$

$$C_2 \equiv \frac{g}{C_p\bar{T}} \left(\frac{d \ln \bar{\theta}}{dz} - \frac{d \ln \kappa}{dz} \right) \quad (36)$$

$$C_3 \equiv -\frac{2C_p\bar{\rho}}{\kappa\Delta t} \quad (37)$$

$$C_4 \equiv \frac{\alpha\bar{\theta}}{g\kappa\bar{T}} \quad (38)$$

The equation we solve during this step is:

$$\begin{aligned} \left(\nabla^2 + C_1 \frac{\partial}{\partial z} + C_2 + C_3 \right) \tilde{\theta}^{N+1} &= (\mathfrak{P}^{N+1} + \mathfrak{P}^N) \\ &\quad - \left(\nabla^2 + C_1 \frac{\partial}{\partial z} + C_2 \right) \tilde{\theta}^N + C_3 \tilde{\theta}^{N+\frac{2}{3}} \end{aligned} \quad (39)$$

This is a second order equation for $\tilde{\theta}^{N+1}$ so we need two boundary conditions to make the solution unique. These come from the requirement that the temperature perturbation on the boundary vanishes: $\tilde{T}|_{\pm \frac{L_z}{2}} = 0$. This requires:

$$\tilde{\theta}^{N+1} \Big|_{\pm \frac{L_z}{2}} = C_4 \left(\tilde{h}^{N+1} - \frac{\mathbf{v}^2}{2} \right) \quad (40)$$

So we see that the differential equation 39 uses only the value of Π^{N+1} , but the boundary conditions need the value of the enthalpy at the updated time. There are two options of how to obtain this value. One is to keep track of the enthalpy from the very beginning and after each pressure step to update it as:

$$\tilde{h}^{N+1} = 2\Pi^{N+1} - \tilde{h}^N \quad (41)$$

However, if the initial value of \hat{h} is not perfectly set this prescription will lead to oscillations in the value of the enthalpy at the top and bottom boundaries. To illustrate this assume that initially we set \tilde{h}^0 to a value that is slightly

higher than what it should be. Since Π^1 is calculated without reference to the initial conditions it will have the correct value. This will lead to \tilde{h}^1 being slightly smaller and so on. These oscillations are then translated to the interior of the box through their effect on the potential temperature variable. Further, we found that these perturbations grow with time for all the cases we ran.

As a result instead of introducing the additional variable \hat{h} with the only purpose of getting temperature boundary conditions we use an approximation to its value through Π :

$$\tilde{h}^{N+1} \approx \frac{1}{2} (3\Pi^{N+1} - \Pi^N) \quad (42)$$

These boundary conditions are then imposed by ignoring the differential equation at the top and bottom wall (where it does not make sense any way) and computing the values of $\tilde{\theta}$ at those boundaries to satisfy the boundary conditions. For the implementation details of this step see appendix B

4. Tests

Since all the Fourier transforms and differential operators are computed in exactly the same way as in Barranco & Marcus (2006), see section 4.1 of that paper for a discussion of the performance of the code.

Below we present various tests we ran to confirm that the code is indeed evolving the equations described above, and that the numerical scheme employed is indeed second order accurate in time. We repeat essentially all the tests that Barranco and Marcus ran to confirm their numerical scheme.

4.1. The background state

Most of the tests we performed have the same background state, which is also the state we used for the final convective box simulation. The only time we modified the background was in order to simulate a convectively stable box and observe g-modes. Here we describe that background state. We use a self consistent non-dimensional set of units. Hence, the results apply for any choice of units.

The dimensions of the box are 4x4x4, with a resolution of 128 collocation points per direction.

Next we need to choose the vertical profile of the heat diffusion coefficient. On one hand, because we require the vertical velocity to vanish at the

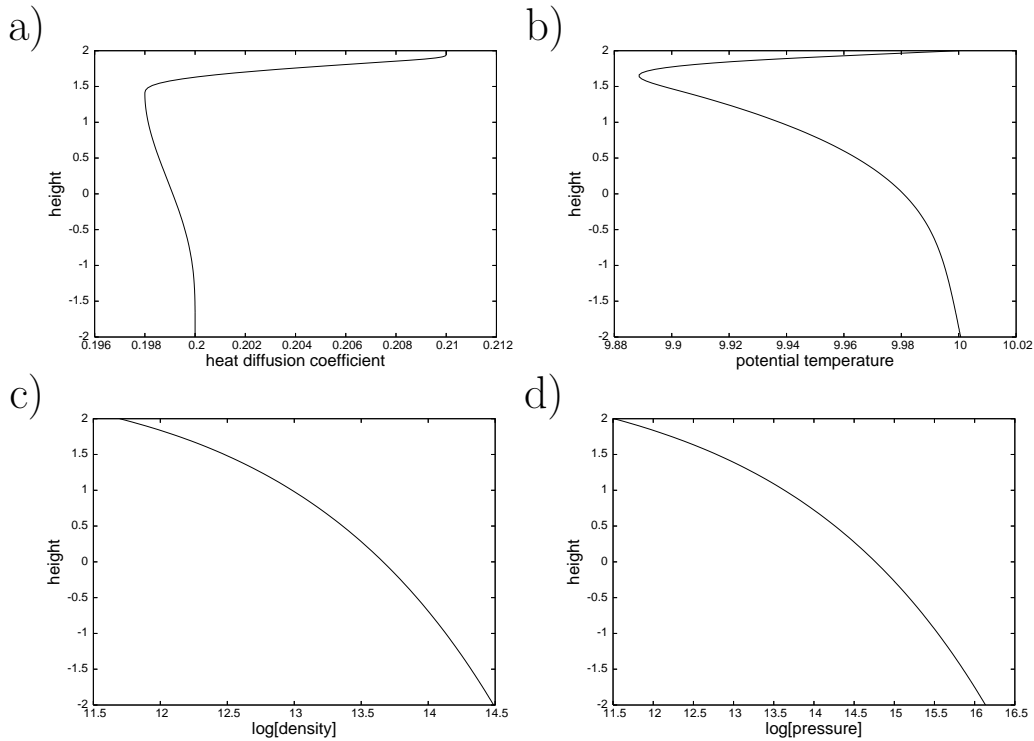


Figure 1: a) The heat diffusion coefficient (κ), b) the background potential temperature ($\bar{\theta}$), c) the background density ($\bar{\rho}$) and d) the background pressure (\bar{p}) profiles.

top and bottom boundaries, we need to set up a background that is stable to convection near those boundaries. On the other hand, we would like to simulate a top-driven convection, which is typical for stars with surface convection zones. To achieve that we need the most unstable stratification to occur near the top of the box. Further, since the heat diffusion step uses the heat diffusion coefficient, and its first and second derivatives, we need our expression for the heat diffusion coefficient to have a continuous second derivative.

To achieve all these requirements we construct the particular $\kappa(z)$ profile

used in this paper from 6 separate pieces as follows:

$$\kappa(z) = \begin{cases} \kappa_0 & , z < z_0 \\ \kappa_1 + \kappa_2 \sin(k(z - z_0)) & , z_0 < z < z_1 \\ \kappa_3 + \kappa_4(z - z_1) \left[\left(\frac{z - z_1}{z_2 - z_1} \right)^2 - 3 \right] & , z_1 < z < z_2 \\ \kappa_5 + \kappa_6(z - z_2)^2 + \kappa_7(z - z_2)^3 + \kappa_8(z - z_2)^4 & , z_2 < z < z_3 \\ \kappa_9 + \kappa_{10} * \sin\left(\pi \frac{z - z_3}{z_4 - z_3}\right) + \kappa_{11}(z - z_3) & , z_3 < z < z_4 \\ \kappa_{12} & , z_4 < z \end{cases} \quad (43)$$

Where the parameters κ_i , $i = 1 \dots 12$, z_j , $j = 1 \dots 4$ and k are chosen to make κ , κ' and κ'' continuous and to select the shape of the curve. The shape of the curve used in this article was determined from the following constraints:

- The values that $\kappa(z)$ takes at the boundaries: $\kappa_0 = 20$ and $\kappa_{12} = 21$.
- The depth above which $\kappa(z)$ remains at its maximum value of κ_{12} : $z_4 = 1.95$.
- The depth at which $\kappa(z)$ has a minimum and the value at that minimum: $\kappa(z_2 = 1.4) = 19.8$
- The depth below which $\kappa(z)$ is held constant at its bottom value of κ_0 : $z_0 = -1.8$
- The locations of the two inflection points: $z_1 = 0.2$ and $z_3 = 1.85$.

A plot of the resulting depth dependence of $\kappa(z)$ is presented in figure 1a.

Next we need to choose values for the background temperature at the top (T_{low}) and bottom (T_{high}) of the box. Those are dictated by the requirement that the flow speeds should never approach the local speed of sound; otherwise, the anelastic approximation is no longer an acceptable approximation and fully compressible equations should be used.

Finally we need to choose values for the pressure at the top of the box (p_{top}), the external gravity (g), the specific heat at constant pressure (C_p), and the value of the ideal gas constant (R). These values, together with T_{low} determine the pressure and density scale heights. Since we are interested in studying turbulence in a stratified medium we need to choose these values

such that our box encompasses at least several pressure and density scale heights. The particular values we chose were:

$$p_{top} = 1.0 \times 10^5 \quad (44)$$

$$g = 2.74 \quad (45)$$

$$C_p = 0.21 \quad (46)$$

$$R = 8.317 \times 10^{-2} \quad (47)$$

$$T_{low} = 10.0 \quad (48)$$

$$T_{high} = 62.37 \quad (49)$$

We deliberately do not include any units in the above quantities, since the simulated flow is independent of the choice of units.

The resulting background potential temperature, pressure and density are presented in figures 1bcd. One can see that the steepest negative slope of $\bar{\theta}$ occurs for heights between 1 and 1.5 units. Also we see we have significant stratification. From figures 1cd we see that the convective box encompasses 2.8 density scale heights and 4.6 pressure scale heights.

4.2. Energy

We first verify that the energy like conserved quantities defined in equation 15 and equation 16 evolve according to equations 17 - 20. The initial conditions we used for this test were that all components of the velocity were set to 0, and the initial potential temperature contained random fluctuations in the lower 10% of the spectral modes. We chose the time step to be much smaller than the smallest absolute value of the buoyancy period, which in this case is an imaginary quantity for most of the box. This way the time step is short both compared to the growth rate of the instability near the middle of the box and the g-mode period near the boundaries.

We perform the test by running the code with no hyperviscosity. We output the kinetic and thermal energies as well as the rates \mathcal{E}_1 and \mathcal{E}_2 at every time step. We then compute the time integrals of \mathcal{E}_1 and \mathcal{E}_2 using Simpson's method. This is sufficient since the numerical evolution is only second order accurate in time. In figure 2 we show that equations 17 - 20 are indeed satisfied to one part in a million.

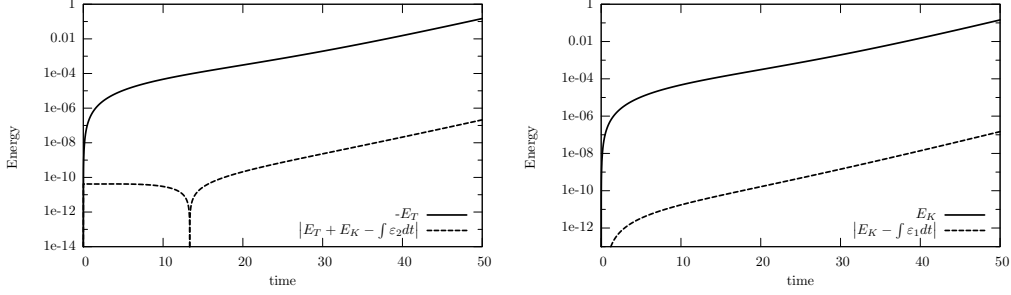


Figure 2: Energy conservation. Left: negative thermal energy – solid line, the absolute difference between the total energy calculated directly and as the integral of \mathcal{E}_2 – dashed line; Right : Kinetic energy (solid line), the absolute difference between the Kinetic energy calculated directly and as the integral of \mathcal{E}_1 – dashed line

4.3. Normal modes

Another test we ran was checking that the normal modes of the linearized equations of motion evolve as expected. We look for normal modes of the form:

$$\tilde{q}(x, y, z, t) = \hat{q}(k_x, k_y, z) e^{-i\omega t + ik_x x + ik_y y} \quad (50)$$

For convenience define

$$\hat{\tau} \equiv g \frac{\hat{\theta}}{\theta} \quad (51)$$

$$\omega_B^2 \equiv g \frac{d \log \bar{\theta}}{dz} = \frac{g}{T} \left(\frac{g}{C_p} - \frac{T_{high} - T_{low}}{L_z} \right) \quad (52)$$

$$(53)$$

In terms of equation 51 and equation 52, and after dropping all nonlinear terms, the anelastic equations (9 – 14) simplify to include only two variables \hat{v}_z and $\hat{\tau}$:

$$-i\omega \left(I - \frac{DD_A}{k_\perp^2} \right) \hat{v}_z = \hat{\tau} \quad (54)$$

$$-i\omega \left[\hat{\tau} + \frac{\kappa R \beta}{C_p \bar{\rho}} (D_A - D) \hat{v}_z \right] = -\omega_B^2 \hat{v}_z + \frac{\kappa}{C_p \bar{\rho}} \left[-k_\perp^2 + \frac{\beta}{T} D + D^2 \right] \hat{\tau} \quad (55)$$

Where the operators D and D_A are defined in appendix A equations 73 and 74.

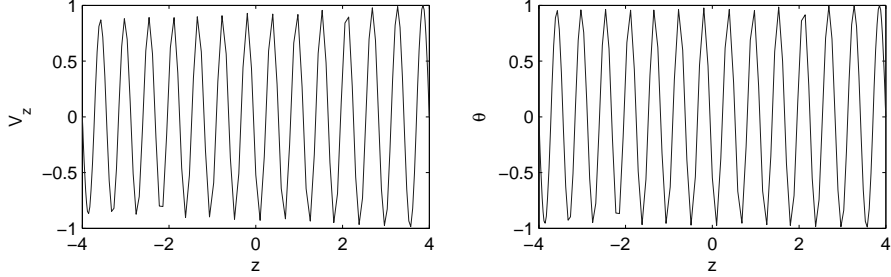


Figure 3: The shape of the normal modes we initialized the box with. On the left is the \hat{z} component of velocity and on the right is the potential temperature.

In terms of \hat{v}_z and $\hat{\tau}$ the remaining flow variables can be expressed as:

$$k_{\perp}^2 \hat{h} = i\omega D_A \hat{v}_z \quad (56)$$

$$i\omega \hat{v}_x = ik_x \hat{h} \quad (57)$$

$$i\omega \hat{v}_y = ik_y \hat{h} \quad (58)$$

We calculated numerical solutions to the eigenmode equations (see figure 3) and supplied them as initial conditions with very low amplitude to the code. We expect that for later times the evolution is done simply by multiplying the initial amplitudes by $e^{-i\omega t}$. We ran the code with the background already discussed above and a time step that was no larger than $\frac{\pi}{250\omega}$ for the mode in question. The comparison with the simulated evolution of these eigenmodes is presented in figure 4. As we can see for large enough time steps the error scales as the square of the time step, which confirms that the code is indeed second order accurate in time. For very small time steps the error deviates from that scaling due to numerical round off. The minimal fractional error is much larger than the numerical precision, because we have chosen the heat diffusion to be as small as possible, which causes the matrix we invert during the heat diffusion step to have values along the diagonal that are many orders of magnitude larger than the off diagonal values, which causes the numerical roundoff to be amplified many times. This also explains why the error in the potential temperature is largest (the other variables suffer from this only indirectly).

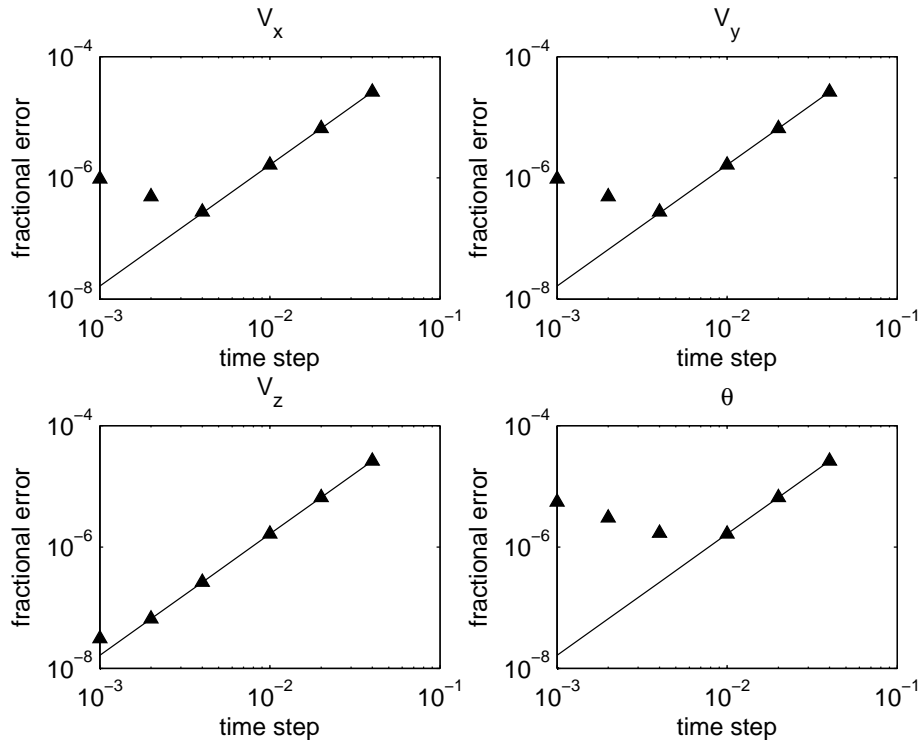


Figure 4: The maximum error in normal mode evolution, after a fixed evolution time. The error is scaled by the maximum value of the quantity at time $t = 0$. The solid line corresponds to quadratic scaling of the error with the time step.

4.4. 2D vortices

Another test we ran was initializing the box with a pair of circular columns of vorticity running from the top to the bottom boundary. In physical space for each column the vorticity was constant and in the \hat{z} direction. The two columns had opposite signs of vorticity so as to ensure that the total vorticity in the box is zero, as required by the periodic boundary conditions. One expects that the two vortices will move parallel at a constant rate determined by the distance between them and the magnitude of their vorticity. Because of the periodic boundary conditions, having two vortices in our box is equivalent to having an infinite number of vortices, copies of the two in the box. There is no analytical expression of the infinite series for the velocity with which each vortex should move, but if the two vortices are far away from the

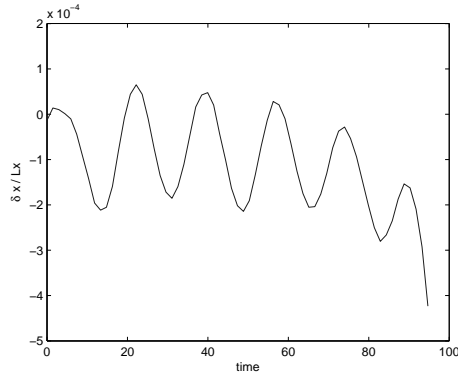


Figure 5: The difference between expected vortex position and the average position of vorticity. The period of the oscillations corresponds to the rotational period of the vortices and the drop in the end is due to the fact that the vortices are exiting the box on the right and hence a bit of them is appearing in the left, causing the average position of vorticity to move toward zero.

walls as compared to the distance between them we expect that their motion is at least approximately that of the situation of only 2 vortices. The time step we chose in this case was $0.01t_{cross}$ (the expected time it would take the vortices to cross half the box). We ran this test and verified that the rate at which the vortices moved corresponded to the approximate analytical rate, see figure 5.

4.4.1. Convectively stable box

The last test we ran was imposing a convectively stable stratification in the box, and initializing with random temperature perturbations. In this case one expects to see g-mode oscillations with a frequency given by the buoyancy frequency $\omega_B^2 \equiv gd \ln \bar{\theta} / dz$. So for this test we needed the buoyancy frequency to be approximately constant throughout the box, and much larger than the time step, but small enough to allow us to simulate many buoyancy periods. So for this test we set the heat diffusion coefficient to be constant throughout the box. Also we set the top and bottom temperatures to be the same. This way the buoyancy frequency was independent of height. The

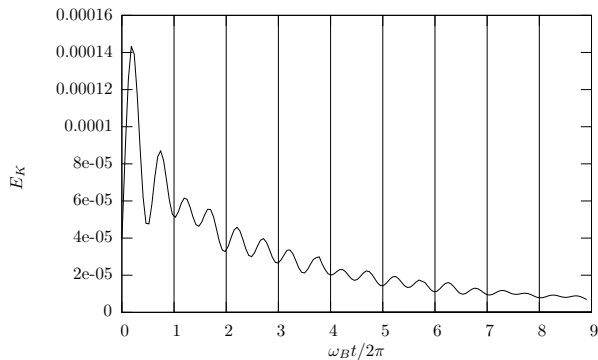


Figure 6: Kinetic energy as a function of time for a convectively stable box. The distance between every two consecutive vertical lines is the buoyancy period. The time is in units where the buoyancy period is 1.

particular values for the parameters of this run were:

$$p_{top} = 1.0 \times 10^5 \quad (59)$$

$$g = 2.0 \quad (60)$$

$$C_p = 0.2 \quad (61)$$

$$R = 8.317e - 2 \quad (62)$$

$$T_{low} = 10 \quad (63)$$

$$T_{high} = 10 \quad (64)$$

$$dt = 0.002 \quad (65)$$

1

This means that the buoyancy frequency is $\omega_B^2 = 2.0$. A plot of the kinetic energy for this run is presented in figure 6. It can be seen that the kinetic energy goes through two cycles every period. This is because the velocity has to go through one cycle, and the energy has a maximum every time the velocity has a maximum or a minimum. The decay in the curve is caused mostly by the heat diffusion smoothing out the perturbations over time. Since different modes decay at different rates and they are coupled through the nonlinear terms we have not shown an expected decay curve.

5. Estimating the dissipation in an unstably stratified convective box

5.1. Steady state flow

Having confirmed that the code is solving the correct equations, we ran a box with the background state described in section 4.1 for long enough to reach a steady-state flow. The criteria for having reached a steady-state flow were that the kinetic and thermal energies should stop drifting systematically up or down (see figure 11). The oscillations we see in the kinetic energy have a period close to the convective turnover time of the box. We also want the spatial spectra of the velocity and potential temperature to be steady to within a few percent. The vertical spectra can not be directly obtained from the output of the simulation since the collocation points of computational grid are not evenly spaced in the vertical direction. So we first had to re-sample to an evenly spaced grid and apply some window function in the vertical direction before performing the discrete Fourier transform. Since in the vertical direction we simulate the Chebyshev series of the quantities the most natural way to re-sample to an even grid was to evaluate this series for each of the new (evenly spaced) collocation points. Fourier power spectra of the 3 velocity components and the potential temperature are presented in figure 7, along with the scaling that Kolmogorov statistics predict (spectral power $\propto k^{-5/3}$). The sharp cutoff at high wavenumbers is related to the resolution of the box (using a box of half the resolution produces a cutoff at half the wavenumber we see in figure 7).

Horizontal cross sections of v_z and $\theta + \bar{\theta}$ at 3 different heights of a typical steady state frame of the flow are presented in figure 8. The three heights we chose were $z = 1.98$, $z = 0$ and $z = -1.98$ for a box in which the vertical coordinate runs from -2 to 2. Horizontal section of the \hat{z} component of the vorticity ω_z as well as typical vertical sections of the above quantities are presented in figure 9.

At the top of the box (figures 8a,d), near the top boundary, the flow exhibits a cellular pattern of narrow downflow lanes. Traces of the cells are visible only in the top 5% of the box, after that the flow organizes itself into a pair of perpendicular downflow lanes that horizontally span the entire box. With time, those lanes get distorted, break up and reform, but are well defined for at least half the time, for most of the upper half of the box. They are generally parallel to the grid axis. Similar patterns were first observed by Porter & Woodward (2000). Their tests show that the lanes tend to align

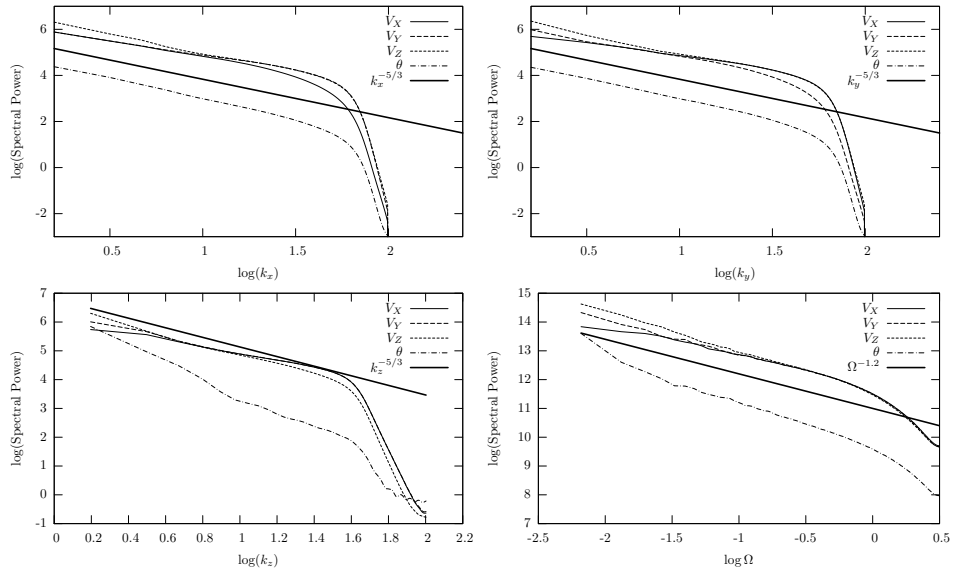


Figure 7: The (x: top left, y: top right, z: bottom left, time: bottom right) spectra of the 3 velocity components and the potential temperature. The thick line in the spatial spectra plots corresponds to Kolmogorov scaling ($E_k \propto k^{-5/3}$). The thick line in the time spectra plot corresponds to the scaling we find for the effective viscosity in the next section.

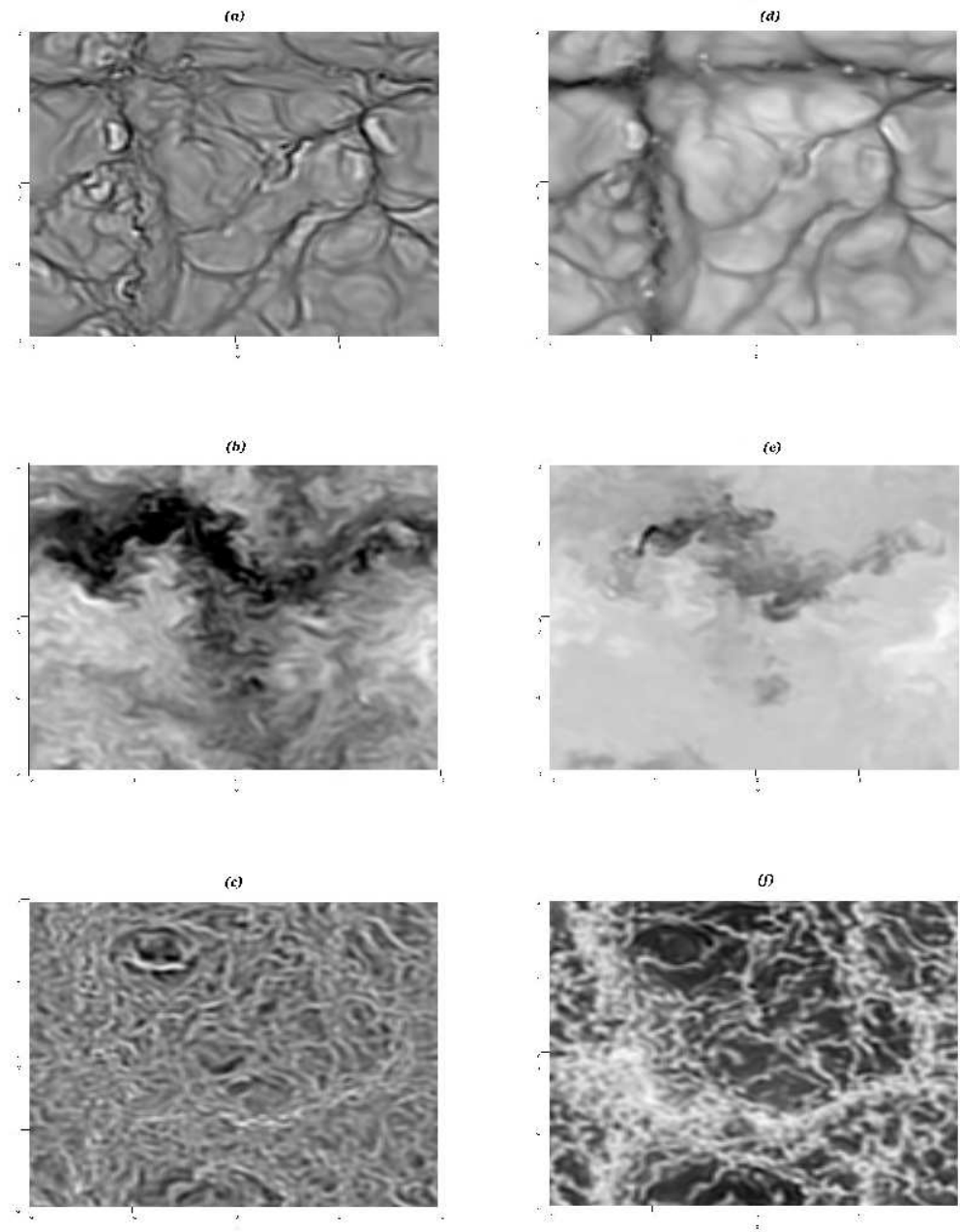


Figure 8: Horizontal cross sections of the vertical velocity component (left) and the total potential temperature (right) at three different heights of the box: $z = 1.98$ (a,d), $z = 0$ (b,e) and $z = -1.98$ (c,f)

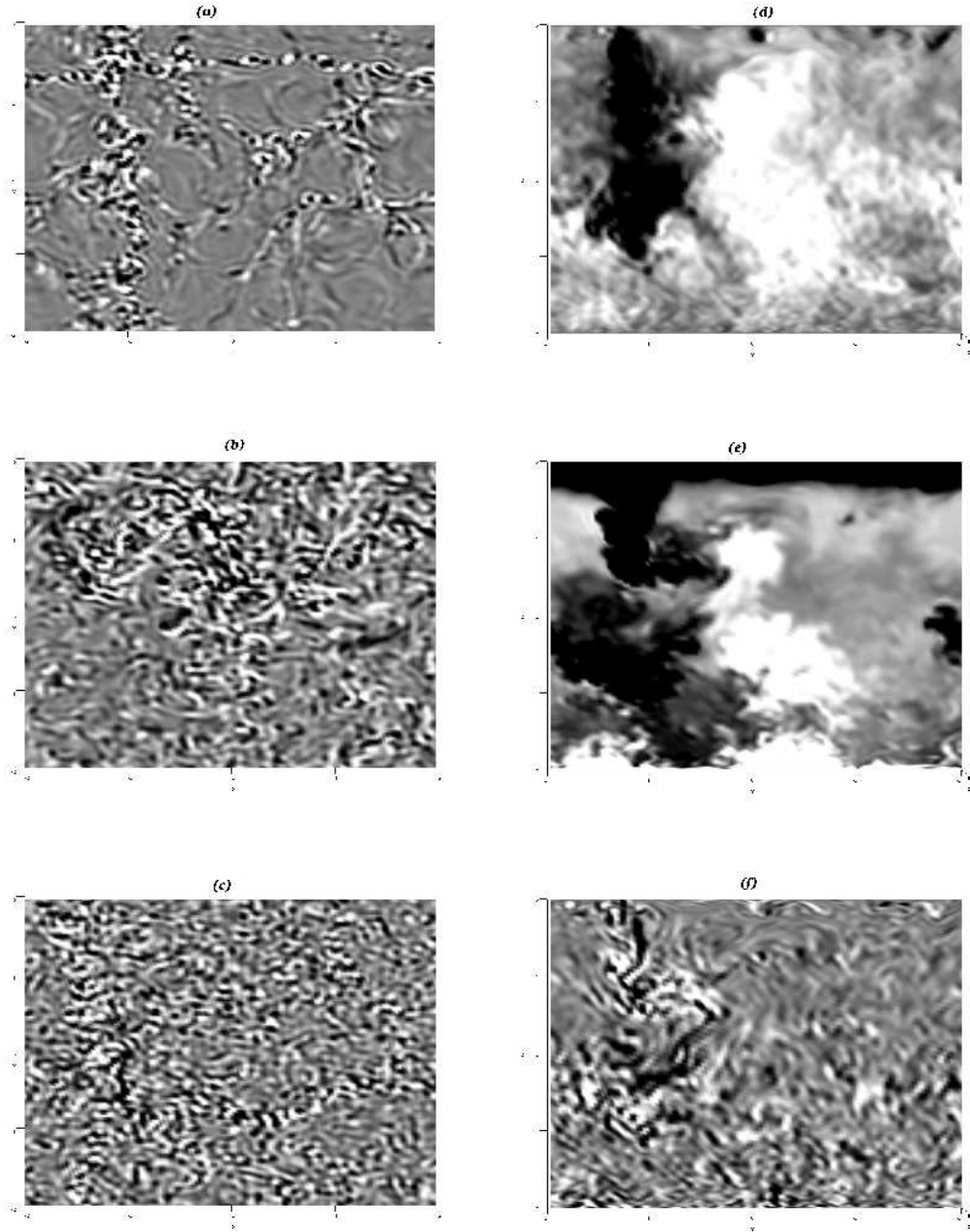


Figure 9: Horizontal cross sections of the vertical vorticity component (left panels) at heights: $z = 1.98$ (a), $z = 0$ (b) and $z = -1.98$ (c). Vertical cross sections (right panels) of the vertical velocity (d), the total potential temperature (e) and the vertical vorticity (f).

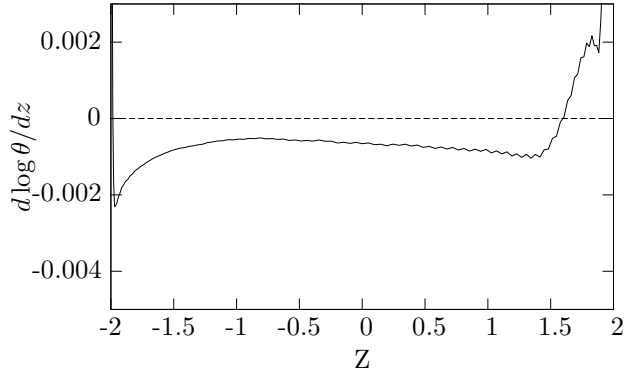


Figure 10: The average logarithmic gradient of the potential temperature.

themselves with the periodic directions of the models, and not with the grid axis per se (rotating the periodic directions at 45° relative to the grid axis caused the lanes to rotate as well). So they conclude this to be due to the small horizontal to vertical aspect ratio of the simulations.

Around the middle of the box the pair of perpendicular lanes are still sometimes visible, but they are a lot less persistent. Rather at those depths the flow consists of one or two downflows, which take up less than a quarter of the cross sectional area among a gentler upflow (figures 8b,e). For the lower half of the box, the asymmetry between up and downflows gradually decreases as we get further down. Near the bottom boundary the large scale of the flow disappears, until only small scale structure is left near the bottom boundary (figures 8c,f).

Since we ran our simulations with the smallest possible value of the heat diffusion coefficient we expect to have very efficient convection, hence we would expect the z gradient of the potential temperature to be very close to zero except near the impenetrable top and bottom boundaries. The averaged over time and horizontal directions logarithmic gradient of $\tilde{\theta} + \bar{\theta}$ can be seen in figure 10. As we can see the scale height of θ is indeed more than two orders of magnitude larger than the box, as long as we are not very close to the boundaries. The top of the box has a local minimum of the entropy gradient and a significant convectively stable region, so as to keep the large magnitude vertical flow from getting too close to the boundary and causing numerical problems. We also see that another local minimum of the entropy gradient has developed near the bottom of the box. This is caused by the

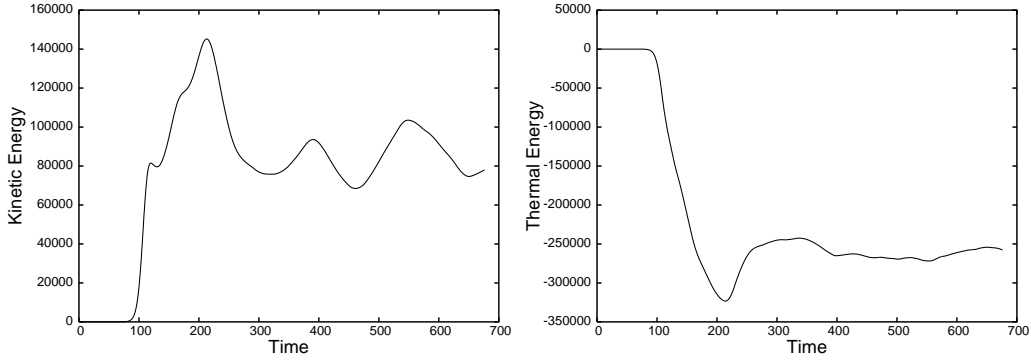


Figure 11: Kinetic (left) and thermal (right) energy content of the convective box used as one of the criteria for having reached a steady state. We decided steady state was reached at time time of 400.

lower impenetrable wall. Not having a significantly thick convectively stable region near the bottom of the box is acceptable, because the larger density of the fluid means that the flow velocities are much smaller at the bottom than at the top of the box.

5.2. Lowest order perturbative expansion

Ignoring the part of the run before steady state was reached we adapted the Goodman & Oh (1997) method as described in Penev et al. (2007, 2008b) to find a lowest order perturbative expansion estimate of the energy transfer rate between a small amplitude external forcing and the turbulent flow in our box, and respectively from that we can derive the components of an effective viscosity tensor that reproduces the energy dissipation rate due to the turbulence. We assume forcing in the form of an external velocity field:

$$\mathbf{V} = \mathbf{A}(t) \cdot \mathbf{x} \quad (66)$$

Goodman & Oh (1997) define two dimensionless parameters: the tidal strain $\Omega^{-1} |\mathbf{A}|$, and $(\Omega \tau_c)^{-1}$, where Ω is the frequency of the perturbation and $\tau_c \equiv L_c/V_c$. The characteristic convective length scale is L_c and V_c is the characteristic convective velocity. In the case of hierarchical eddy structured convection τ_c is the largest eddy turnover time.

We then take only the lowest nonzero term in the expansion of the secular rate of change of the kinetic energy $\dot{\mathcal{E}}$ with respect to those two parameters.

(Penev et al., 2008b) adapt the (Goodman & Oh, 1997) formalism for discretely sampled data on a finite spatial and temporal domain the resulting expression is:

$$\begin{aligned} \dot{\mathcal{E}}_{2,2}(\Omega = 2\pi R/T) = & \frac{2T}{\mathcal{N}^2 N_z} \sum_{\lambda, \mu, \nu, \nu'} Re \left\{ \hat{\rho}_{\nu-\nu'}^* \left[\hat{\mathbf{v}}_{\lambda, \mu, \nu, -R} \cdot \hat{\mathbf{A}}(\Omega) \mathbf{P}_{\lambda, \mu, \nu'} \hat{\mathbf{A}}(-\Omega) \cdot \hat{\mathbf{v}}_{\lambda, \mu, \nu', -R}^* \right] \right\} \\ & - \frac{4}{\mathcal{N}^2 N_z} \sum_{\lambda, \mu, \nu, \nu'} \sum_{\rho \neq 0} \frac{1}{\omega_\rho} Im \left\{ \hat{\rho}_{\nu-\nu'}^* \left[\hat{\mathbf{v}}_{\lambda, \mu, \nu, \rho-R} \cdot \hat{\mathbf{A}}(\Omega) \mathbf{P}_{\lambda, \mu, \nu'} \hat{\mathbf{A}}(-\Omega) \cdot \hat{\mathbf{v}}_{\lambda, \mu, \nu', \rho-R}^* \right] \right\} \end{aligned} \quad (67)$$

Where the simulations are assumed to span a time in the range of $(0, T)$; N_x , N_y , N_z and N_t are number of grid points in the x , y , z and time directions respectively; $\mathcal{N} \equiv N_x N_y N_z N_t$, λ, μ, ν, ρ are indices for grid points in discrete Fourier space: $\mathbf{k}_{\lambda, \mu, \nu} \equiv (2\pi\lambda/L_x, 2\pi\mu/L_y, 2\pi\nu/L_z)$, $w_\rho \equiv 2\pi\rho/T$; $\hat{\mathbf{v}}$ is the time and space Discrete Fourier Transform (DFT) of the convective velocity in the absence of the external perturbation (i.e. the simulated velocity field); $\hat{\rho}$ is the DFT of the background density along the z direction; $P_{\lambda, \mu, \nu} \equiv \mathbf{I} - \mathbf{k}_{\lambda, \mu, \nu} \mathbf{k}_{\lambda, \mu, \nu} / k_{\lambda, \mu, \nu}^2$ is the discrete version of the P_k operator defined by (Goodman & Oh, 1997) that maintains incompressibility.

The 2, 2 subscripts of $\dot{\mathcal{E}}_{2,2}$ denote that equation 67 contains up to second order terms in the two dimensionless parameters characterizing the tide and the convection respectively, $\rho(k_z)$ is the Fourier transform of the density averaged over x, y, t . The normalization is such that $\rho(0)$ is the average density over all space and time.

To perform the calculation we use a discreet Fourier transform to estimate the spectra of the velocities and density needed in equation 67, but before that we again re-sample to a grid that has its collocation points evenly spaced in the vertical direction. We have to be careful when using discreet Fourier transforms to estimate spectra. In particular we need to pay special attention to the z and time directions, since they are not periodic and hence the discreet Fourier transforms suffer from windowing effects. To confirm that our results are not significantly affected, we perform the same calculations using no windowing in those two directions, as well as Welch (parabolic) and Bartlett (triangular) windows. Also it is possible that the impenetrable top and bottom walls might influence our result. So we also tried a Welch and Bartlett window functions that exclude the top 12.5% and the bottom 5%. The resulting effective viscosity scalings from all these tries were not significantly different.

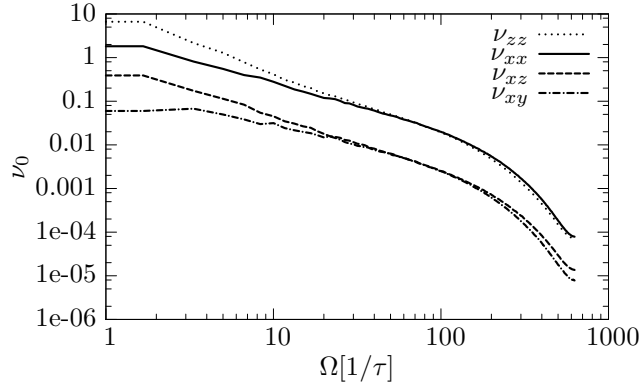


Figure 12: The four independent components of the viscosity tensor as estimated by the Goodman & Oh (1997) method. The vertical axis is the effective viscosity in units of $\langle v_z^2 \rangle^{1/2} H_p$ (H_p - pressure scale height) and the horizontal axis is the perturbation frequency in units of inverse convective turnover time (τ).

We then note that the energy transfer rate of equation 67 is due to the external forcing. If the flow is steady state this transfer rate must be balanced by the energy dissipated by the turbulence. We can then extract the different components of the effective viscosity by setting all terms of \mathbf{A} to zero except for one, and matching to the energy dissipation rate that an actual molecular viscosity (ν) would cause:

$$\dot{\mathcal{E}}_{visc} = \frac{1}{2} \langle \rho \nu \rangle \text{Trace} [\mathbf{A}(\Omega) \cdot \mathbf{A}^*(\Omega)], \quad (68)$$

where averaging is done over the volume of the box and over time. Note that this is only the dissipation of the flow caused by the external shear. In the absence of external shear (i.e. $\mathbf{A} \rightarrow 0$) there is no dissipated energy. The dissipation of the convective flow is not of interest because it is assumed to be balanced by the thermal driving of the convection.

Since physically there should be no difference between the two horizontal directions we expect that $\nu_{xx} \approx \nu_{yy}$, $\nu_{xy} \approx \nu_{yx}$ and $\nu_{xz} \approx \nu_{yz} \approx \nu_{zx} \approx \nu_{zy}$. We verified that these approximations indeed hold. So we are left with only four independent components of the viscosity tensor. Those are presented in figure 12. As we can see, all the components have similar scaling with frequency, and the diagonal components are a bit over an order of magnitude larger than the off-diagonal components. The approximate frequency scaling

for the low frequency dependence of the viscosity components (for $\Omega < 100$) is:

$$\nu \propto \Omega^{1.2 \pm 0.1} \quad (69)$$

6. Conclusion

The above result points to the possibility that viscosity in turbulent convection zones loses efficiency significantly slower than what Kolmogorov scaling predicts at least on large timescales. This seems to be due to the fact that the turbulent eddies with turnover times similar to these large timescales are not in the inertial subrange and hence, the velocity power spectrum is much shallower than the Kolmogorov 5/3 law. This result is not conclusive, since the possibility remains that dropping higher order terms in the above expansion is not a good approximation.

In Penev et al. (2008a) we introduce horizontal depth dependent forcing into the flow equations and obtain the dissipation properties of the turbulent convective flow directly. We were then able to compare the average rate of work done on the flow by the external forcing to the expected rate of energy transport and dissipation by an assumed effective viscosity. We found that with sufficiently long time average these two quantities have the same depth dependence, thus verifying the validity of the assumption that an effective viscosity coefficient is sufficient to parametrize the average dissipation and momentum transport properties of the turbulent convective flow. Further, by repeating the above procedure a number of times we were able to derive the scaling of this effective viscosity coefficient with period and confirm that it is linear.

In this paper we have presented a code that is well suited for the purpose of studying turbulent dissipation in convective zones. First it is a spectral code, which means that the spatial accuracy is exponential, and hence the code efficient for simulating turbulent flows. Further by using the anelastic approximation we do not need to deal with sound waves and shocks. This allows us to take much larger time steps (by more than an order of magnitude) than with a fully compressible code, and hence we can have runs that cover a much longer physical time than fully compressible simulations. This is important since the external forcing regimes we are interested in are tides with orbital periods of several days, which is not achievable in reasonable time with fully compressible codes.

The price we pay of course is that the flow we simulate is not a good approximation to the flow in any star’s surface convection zone. Firstly, we cannot accommodate the region where the driving of the convection occurs, because this region is characterized by strongly supersonic flows and shocks, also the mean free path of light in that region is not small and hence the radiative effects can no longer be captured by a heat diffusion coefficient. Secondly, our code uses the ideal gas equations of state which is a poor approximation to the upper layers of stars.

However, the scaling of the effective viscosity with frequency we obtained (equation 69) for our box agrees with the scalings obtained with the same perturbative approach applied to realistic simulations of the upper layers of the convection zones of the sun and two smaller stars (Penev et al., 2007, 2008b). Which gives us confidence that our results are applicable to the systems we are interested in studying.

We would like to acknowledge the contribution of Philip Marcus to the development of the original code (Barranco & Marcus, 2006).

A. Implementing the Pressure Step

As discussed in section 3.2.3 in order to advance the enthalpy by one time step we need to solve the following differential equation with boundary conditions:

$$\begin{aligned} \left[\nabla^2 + \frac{d \log \bar{\rho}}{dz} \frac{\partial}{\partial z} \right] \Pi^{N+1} &= \frac{1}{\Delta t} \left(\nabla \cdot \mathbf{v}^{N+\frac{2}{3}} + v_z^{N+\frac{2}{3}} \frac{d \log \bar{\rho}}{dz} \right) \\ \frac{\partial \Pi^{N+1}}{\partial z} \Big|_{\pm L_z/2} &= \frac{1}{\Delta t} v_z^{N+\frac{2}{3}} \Big|_{\pm L_z/2} \end{aligned} \quad (70)$$

The solution is obtained in two steps. First we impose the boundary conditions by ignoring the differential equation for the two highest Chebyshev modes and replacing it with the equations for the boundary conditions. Then we use a Green’s step (see sec. A.1) to fix the equation for those two highest modes and instead impose the boundary conditions at the expense of satisfying the equation at the physical top and bottom boundary.

We need to solve this equation as efficiently as possible. Clearly we can make this a trivial matrix multiplication operation if we were to store the inverse of the left hand side operator for each horizontal mode at the start, and at each time step we multiply every vertical slice of the transformed right

hand side by the corresponding inverse to get the value of Π^{N+1} . However, this would require a $N_x \times N_y$ matrices of N_z^2 elements to be stored (where N_x , N_y and N_z are the resolutions in the \hat{x} , \hat{y} and \hat{z} directions respectively), which for large resolutions is likely to exceed the amount of memory available on each node of the cluster where the code is to run.

To avoid this we need to find the most efficient way which only stores things common to all horizontal modes. We see that the pressure equation is almost identical for all horizontal modes, except for the horizontal component of the ∇^2 operator, which in Fourier space means simply multiplying by $k_\perp^2 \equiv k_x^2 + k_y^2$, where k_x and k_y are the corresponding \hat{x} and \hat{y} wavenumbers for each mode. So what we can reasonably do is pre-compute the common part of the left hand side operator and then for each horizontal mode add k_\perp^2 along the diagonal. We then overwrite the last row of the resulting matrix ($\mathbf{M}_{i,j}$) with

$$M_{N_z,p} = p^2 \quad (71)$$

$$M_{N_z-1,p} = (-1)^p p^2 \quad (72)$$

in order to impose the boundary conditions. We then decompose \mathbf{M} into an upper and lower triangular parts and solve by backward substitution. The right hand side vector also needs to have its highest two entries overwritten with the boundary conditions at the top and bottom of the box respectively.

A.1. Green's Step

In this step we fix the anelastic constraint even for the two highest Chebyshev modes and instead break the two highest modes of the momentum equation to satisfy the boundary conditions which we break in the process. To make expressions shorter define the following operators:

$$D \equiv \frac{d}{dz} \quad (73)$$

$$D_A \equiv \frac{d}{dz} + \frac{d \ln \bar{\rho}}{dz} \quad (74)$$

$$\nabla \equiv ik_x \hat{\mathbf{x}} + ik_y \hat{\mathbf{y}} + D \hat{\mathbf{z}} \quad (75)$$

$$\nabla_A \equiv ik_x \hat{\mathbf{x}} + ik_y \hat{\mathbf{y}} + D_A \hat{\mathbf{z}} \quad (76)$$

$$\Delta_A \equiv \nabla_A \cdot \nabla \quad (77)$$

We would like to modify the pressure step in a way that will include two new degrees of freedom which we can then use to fix the anelastic constraint for

the two highest Chebyshev modes. The particular modification useful in this case is:

$$\mathbf{v}^{N+1} = \mathbf{v}^{N+\frac{2}{3}} - \Delta t \nabla \Pi^{N+1} + \hat{\mathbf{z}} (\tau_1^{N+1} T_{M-1} + \tau_2^{N+1} T_M) \quad (78)$$

Where T_N denotes a Chebyshev polynomial of order N , τ_1 and τ_2 are arbitrary coefficients to be chosen later and M is the order of the highest Chebyshev coefficient we are simulating.

Requiring the anelastic constraint and velocity boundary conditions gives:

$$\Delta_A \Pi^{N+1} = \frac{1}{\Delta t} \nabla_A \cdot \mathbf{v}^{N+\frac{2}{3}} + \tau_1^{N+1} D_A T_{M-1} + \tau_2^{N+1} D_A T_M \quad (79)$$

$$D \Pi^{N+1} \Big|_{\pm L_z/2} = \frac{1}{\Delta t} v_z^{N+\frac{2}{3}} + \tau_1^{N+1} T_{M-1} + \tau_2^{N+1} T_M \Big|_{\pm L_z/2} \quad (80)$$

To proceed we break up Π^{N+1} into 3 pieces:

$$\Pi^{N+1} = \Pi_0^{N+1} + \frac{1}{\Delta t} (\tau_1^{N+1} \Gamma_1^{N+1} + \tau_2^{N+1} \Gamma_2^{N+1}) \quad (81)$$

This allows us to split the above equation into 3 separate equations with corresponding boundary conditions, the first of which is the already calculated pressure step:

$$\Delta_A \Pi_0^{N+1} = \frac{1}{\Delta t} \nabla_A \cdot \mathbf{v}^{N+\frac{2}{3}} \quad (82)$$

$$D \Pi_0^{N+1} \Big|_{\pm L_z/2} = \frac{1}{\Delta t} v_z^{N+\frac{2}{3}} \Big|_{\pm L_z/2} \quad (83)$$

$$\Delta_A \Gamma_1^{N+1} = D_A T_{M-1} \quad (84)$$

$$D \Gamma_1^{N+1} \Big|_{\pm L_z/2} = T_{M-1} \Big|_{\pm L_z/2} \quad (85)$$

$$\Delta_A \Gamma_2^{N+1} = D_A T_M \quad (86)$$

$$D \Gamma_2^{N+1} \Big|_{\pm L_z/2} = T_M \Big|_{\pm L_z/2} \quad (87)$$

We solve the two new equations the same way we solve the first. This makes as before the anelastic constraint satisfied for all but the two highest Chebyshev modes, but this time we have 2 arbitrary constants τ_1 and τ_2 which we can then set to values that will make the anelastic constraint hold for those two modes as well.

B. Implementing the Heat Diffusion Step

The same considerations as the pressure step apply to this step. We again decide against making a table of pre-inverted matrices for each horizontal mode, and instead we only pre-compute the part of the matrix that is common for all horizontal modes. To make the description of the numerical procedure followed we define the following matrices:

CP : transforms a vector from Chebyshev to physical space

PC : transforms a vector from physical to Chebyshev space

D : differentiates a vector in Chebyshev space

From those we construct a derivative operator and the common part of the left hand side operator, both in physical space:

$$D_P \equiv CP \cdot D \cdot PC \quad (88)$$

$$M_P \equiv D_P \cdot D_P + F \cdot D_P + G \quad (89)$$

What we pre-compute and store is a matrix \mathbf{M} , which we obtain by overwriting the first and last row of M_P with:

$$M_{P1,1} = 1 \quad M_{P1,j} = 0, \quad j = 2..N_z \quad (90)$$

$$M_{PN_z,j} = 0, \quad j = 1..N_z - 1 \quad M_{PN_z,N_z} = 1 \quad (91)$$

to allow for imposing the boundary conditions, then sandwiching the resulting matrix between PC and CP :

$$\mathbf{M} \equiv PC \cdot M_P \cdot CP \quad (92)$$

Then in order to solve equations 39 and 40 for each horizontal mode we construct a new matrix $\mathbf{M}'(k_\perp)$ from \mathbf{M} as follows:

$$\mathbf{M}'_{i,j}(k_\perp) \equiv \mathbf{M}_{i,j} - k_\perp^2 \delta_{i,j} + k_\perp^2 (PC_{i,0}CP_{0,j} + PC_{i,N_z-1}CP_{N_z-1,j}) \quad (93)$$

The first new term adds the horizontal part of the ∇^2 operator for the given mode. However, this breaks the requirements for the boundary conditions, so we repair them with the other two terms. This way the boundary conditions are directly imposed by breaking equation 39 at the physical top and bottom of the box, instead of ignoring it for the two highest Chebyshev modes. That means we do not need to perform extra greens steps like we did for the pressure equation. Then we obtain the solution to equation 39 by decomposing $\mathbf{M}'(k_\perp)$ into an upper and lower triangular matrices and using back-substitution.

References

- Bannon, P. R. 1996, *J. Atmos. Sci.*, 53, 3618
- Barranco, J. A. & Marcus, P. S. 2006, *J. Comp. Phys.*, 219, 21
- Goldreich, P. & Keeley, D. A. 1977, *ApJ*, 211, 934
- Goldreich, P. & Kumar, P. 1988, *ApJ*, 326, 462
- Goldreich, P., Murray, N., & Kumar, P. 1994, *ApJ*, 424, 466
- Goldreich, P. & Nicholson, P. D. 1977, *Icarus*, 30, 301
- Gonczi, G. 1982, *A&A*, 110, 1
- Goodman, J. & Oh, S. P. 1997, *ApJ*, 486, 403
- Malagoli, A., Cattaneo, F., & Brummell, N. H. 1990, *apjl*, 361, L33
- Meibom, S. & Mathieu, R. D. 2005, *ApJ*, 620, 970
- Penev, K., Barranco, J., & Sasselov, D. 2008a, [arXiv:0810.5370](https://arxiv.org/abs/0810.5370)
- Penev, K., Sasselov, D., Robinson, F., & Demarque, P. 2007, *ApJ*, 655, 1166
- . 2008b, [ArXiv e-prints](https://arxiv.org/)
- Porter, D. H. & Woodward, P. R. 2000, *ApJS*, 127, 159
- Sofia, S. & Chan, K. L. 1984, *apj*, 282, 550
- Stein, R. F. & Nordlund, A. 1989, *ApJ*, 342, L95
- Verbunt, F. & Phinney, E. S. 1995, *A&A*, 296, 709
- Zahn, J. P. 1966, *Ann. d'Astrophys.*, 29, 489
- Zahn, J. P. 1989, *A&A*, 220, 112